Acta Materialia 268 (2024) 119732

Contents lists available at ScienceDirect

Acta Materialia

journal homepage: www.elsevier.com/locate/actamat

Full length article

Influence of variation in grain boundary parameters on the evolution of atomic structure and properties of [111] tilt boundaries in aluminum

Saba Ahmad *, Tobias Brink, Christian H. Liebscher, Gerhard Dehm

Max-Planck-Institute für Eisenforschung GmbH, Max-Planck-Straße 1, Düsseldorf 40237, Federal Republic of Germany

ARTICLE INFO

Keywords:
Aluminium
High-angle grain boundaries
Atomically resolved structure
Structure-property correlation
Scanning transmission electron microscopy (STEM)
Atomistic simulation

ABSTRACT

Grain boundaries (GBs) are fundamental planar defects in metallic materials, exerting a profound influence on material behaviour and properties. Understanding the influence of GB structure on material performance presents challenges due to the intricate atomic arrangements involved. To overcome inconsistencies observed in previous simulations, experimental validation is necessary. However, research on [111] tilt GBs in metals other than copper, such as aluminium, remains limited. This study aims to address these gaps by investigating the characterization of [111] tilt GBs in Al, employing advanced experimental techniques and validating the findings through simulations. By exploring a range of misorientation angles and plane inclinations, two distinct misorientation groups are identified, each exhibiting unique structural configurations. However, the structural differences resulting from plane inclination are more pronounced than those stemming from misorientation angle. Additionally, it is found that deviations from precise misorientation angles and different plane inclinations significantly influence the excess properties of GBs, such as GB energy and excess volume, etc. Furthermore, comparisons between Al and Cu structures enhance our understanding of GB behaviour in different metallic materials. This study lays the foundation for robust structure-property correlations in GBs and emphasizes the importance of considering intricate GB structural details to better understand and predict their properties accurately.

1. Introduction

In metallic materials, grain boundaries (GBs) are common planar defects and exhibit distinct crystallographical and compositional characteristics from the bulk [1]. Several processes that can alter the properties of the interfaces, dramatically affect the behavior of polycrystalline materials such as change in GB diffusivity due to structural transitions at the GB [2], abnormal grain growth due to the presence of two different GB structures (with different mobility) [3], and embrittlement of Cu GBs caused by Bi segregation [4]. Furthermore, each GB is distinguished by its unique thermodynamic excess properties that are controlled by the local atomic structure and chemistry of a GB [5–10]. It is currently challenging to relate material performance to its internal GB structure. This is because a large number of GBs could exist in a system with several complicated atomic structures (resulting from varying macroscopic parameters), at constant thermodynamic variables. The trends by which GB structures and their corresponding properties vary with the GB macroscopic parameters must therefore be understood on a broad scale.

In the last few decades, numerous studies [11–19] explored the atomic structures of several coincidence-site lattice (CSL) GBs and their properties in a variety of fcc materials, however usually by employing atomistic simulations. It has been found that the modeled structures from several simulations [12,15,17] for the same GB type are inconsistent with one another. This makes it difficult to understand which GB structures truly exist in reality. Combining the results of the calculated boundary structures with relevant experimental observation has resulted in new discoveries, such as the possibility of the co-existence of two or more different structures at the GB and their correlation to the GB properties [20–24]. However, very few of these investigations have been conducted for [111] type tilt GBs [25,26]. Meiners et al. [25] conducted one such study at a Σ19b [111] {1 7 8} GB, where they employed atomic-resolution imaging and molecular dynamics modeling to investigate the existence of two unique GB structures/phases (i.e. pearl and domino) and their transformation kinetics. Similar structures were found at the Σ37c [111] {1 10 11} GB [26]. It's important to consider that the majority of experimental research on [111] tilt GBs is done for Cu. Therefore, to achieve a comprehensive understanding of GBs in

* Corresponding author.
E-mail address: saba@mpie.de (S. Ahmad).

https://doi.org/10.1016/j.actamat.2024.119732
Received 26 October 2023; Received in revised form 1 February 2024; Accepted 4 February 2024
Available online 5 February 2024

various fcc metal systems, such as Al, it is essential to investigate their actual structures and verify the predictions made by molecular dynamics (MD) simulations [16].

Furthermore, it is also important to recognize that just a small number of distinct [111] tilt GBs have been the focus of experimental investigation [25–29]. Even a small misorientation variation has an impact on GB attributes due to the incorporation of steps, defects, or additional structural units into the GB. Hence, it is of great interest to empirically investigate the structures of several different GBs with different misorientation in order to establish the structure-property correlation. To the authors' knowledge, no experimental studies have been conducted to determine how the change in the misorientation angle alters the atomic structure of [111] tilt GBs in pure fcc metals. Furthermore, previous studies [9,27,30] suggest that modifying the GB plane could potentially lead to entirely new atomic structures with distinct properties. Consequently, it is also necessary to examine the structure of GBs with a fixed misorientation but different boundary planes.

In the current study, we have thus examined the atomic structures of various [111] tilt GBs (Σ21a, Σ13b, Σ7, Σ19b, Σ37c and Σ3) described by misorientation angle (θ) and a particular inclination of the boundary plane by using aberration corrected scanning transmission electron microscopy (STEM) and atomistic simulations. We found that these GBs could be categorized into two distinct misorientation groups, each characterized by different structural units (SUs). While some of the boundary structures have been previously explored in the literature for Cu, this study extends the analysis by comparing them to the corresponding structures in Al. Furthermore, our study investigated how the structural units (SUs) at the GBs varied when there was a slight deviation from the ideal misorientation angle and a change in the GB plane inclination. We examined the influence of these variations on the excess properties of the GBs. Our findings revealed that the intricate details, such as the specific misorientation angle and inclination of the GB plane, significantly influence these properties.

2. Methods

2.1. Experimental methods

The GBs investigated in this paper were extracted from a pure Al thin film (approximately 800 nm in thickness) grown by magnetron sputtering. Using electron backscatter diffraction (EBSD), the microstructural characteristics of the films, including texture, GB character, and distribution, were studied, as described in Ref. [28]. Plane-view TEM lamellas comprising several special GBs were prepared by a site-specific plasma focused ion beam (PFIB) lift-out using a dual beam SEM / FIB instrument Helios G3 Cx (Thermo Fischer Scientific). Due to the challenging sample preparation by PFIB, the success rate of producing a decent TEM specimen is quite low. Additionally, only 12 out of the 20 good quality specimens yielded successful results, mostly due to localized deviations from the desired edge-on conditions of the boundaries. Here, special GBs refer to the coincidence site lattice (CSL) boundaries, where Σ defines the ratio of the coincidence lattice sites to the total number of lattice points. Note that the experimentally observed GBs are geometrically represented here by different Σ values for simplicity. However, the distinction cannot simply be made on the basis of this straightforward geometrical CSL model [31], because in reality the GBs deviate from their nominal misorientation, as illustrated in Table 1. Hence, in the end we need distinction through the structural unit characterization from the experimentally observed structures.

Atomistic characterization of the TEM sample was conducted by high-angle annular dark field (HAADF) scanning transmission electron microscopy (STEM) using a probe-corrected FEI Titan Themis 60-300 (Thermo Fischer Scientific) S/TEM, equipped with a high-brightness field emission gun (FEG) and a gun monochromator operated at 300 keV. The semi-convergence angle was set to either 17 mrad or 23.8 mrad with a probe current of typically greater than 80 pA. All HAADF images were recorded with a collection angle range of 78 mrad–200 mrad and 40 mrad–200 mrad by altering a camera length between 100 mm and 190 mm. In our study, we primarily focused on examining symmetric GBs along the [111] tilt axis. Geometrically, two crystallographically distinct sets of symmetric GB planes can be constructed, resulting in two symmetric GB variants. For instance, in the case of the Σ19b boundary, the {352} symmetric planes and the {178} symmetric planes represent distinct symmetric variants (i.e. variant I and II) of the GB, as depicted in Fig. 1.

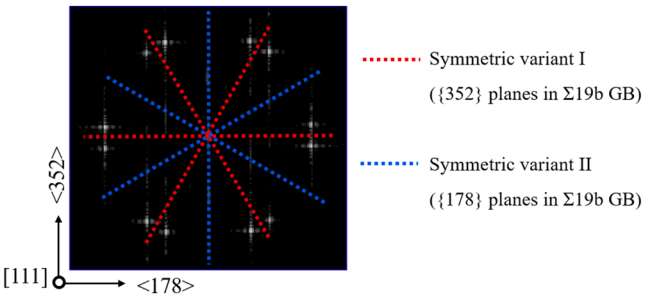

Fig. 1. Fast Fourier Transform (FFT) of a Σ19 [111] tilt GB. Two adjacent grains are oriented along the [111] zone axis and rotated with regard to each other. The Σ19 boundary has two symmetric variants corresponding to {352} and {178} GB planes, as represented by dashed red and blue lines, respectively. With respect to the symmetric variant I, the GB plane for the symmetric variant II is rotated by 30°. (For interpretation of the references to colour in this figure legend, the reader is referred to the web version of this article.)

2.2. Simulation methods

In order to obtain 3D information about the atomic structures, have exact control over misorientation and inclination, and to extract GB excess properties, we also performed atomistic simulations. We used an embedded atom method (EAM) potential for Al [33] for molecular statics and molecular dynamics (MD) simulations using LAMMPS [34,35]. GB structures at $T = 0$ K were produced by joining bicrystals at the desired crystal planes, sampling different displacements between the crystallites, and minimizing the atomic positions with regard to the potential energy of the system (γ-surface method). The GB planes for different Σ GBs were calculated using the software GB code [36]. The simulation cells contained 1000–2000 atoms.

Structures were compared to the experimental images and the low-energy structures matched between experiment and simulation, except where noted otherwise in the text. Thermodynamic excess properties were calculated as described in Refs. [37,38]. Here, we use the GB excess energy

$$\gamma = \frac{E - N\frac{E_{\mathrm{ref}}}{N_{\mathrm{ref}}}}{A} \tag{2.1}$$

and the excess volume

$$[V] = \frac{V - N\frac{V_{\mathrm{ref}}}{N_{\mathrm{ref}}}}{A} \tag{2.2}$$

The energy E and volume V are calculated for a region with N atoms containing a GB with GB area A. The reference values E_{ref} and V_{ref} are calculated in a defect-free system with N_{ref} atoms. Note that we deviate from Refs. [37,38] by including the normalization by GB area in the excess values for simplicity of notation. Finite temperature effects on the structures were investigated by scaling the lattice constants of the simulation cells and then running MD simulations for 1 ns using a Langevin thermostat at 300 K with a time step of 2 fs. Atomic positions were averaged over the last 250 ps of the simulation to obtain the results in the Appendix.

3. Results and interpretation

3.1. Atomic structures of symmetric variant I of Σ21a, Σ13b, Σ7, Σ19b, Σ37c and Σ3 GBs

Figs. 2 and 3 show the atomic structures of variant I of six symmetric [111] tilt GBs (Σ21a, Σ13b, Σ7, Σ19b, Σ37c and Σ3) as a function of misorientation angle (Experimental θ), as described in Table 1.

The characteristic SUs are used to describe the complete atomic structure of all the Σ GBs [13,39]. According to the SU model specification [13], the GB structure for Σ21a, Σ13b and Σ7 can be written as |AAB|, |AAB'| and |B|, where B and B' represent the similar types of bow-and-arrow shaped red sub-units. In the projection, the atomic structure of Σ21a {134} and Σ13b {134} is comprised of two types of the sub-units (i.e. A and B/B'), as highlighted by red circles and green circles, in Fig. 2, respectively. The red sub-unit of the symmetric Σ21a {134} GB with a misorientation of 25°, exhibits a bow and arrow shape formed by 11 atomic columns while the green sub-units (A) are formed by 3 atomic columns.

In case of Σ13b {134} with a misorientation of 27°, the red sub-unit appears different to the Σ21a structure and possesses a distorted bow and arrow shape with an extra atomic column in the center of the GB (highlighted in yellow with total 12 atomic columns). The presence of this extra atomic column in the SUs of Σ13b makes it denser as compared to the SUs of Σ21a. This introduces a change in the inner structure of the primary structural units in the Σ13b (27°) GB. However, the outer shape of the structural unit remains the same. Hence, the bow and arrow structural units are designated as B'. Additionally, the atomic structure of the Σ7 (34°) GB consists mainly of the same unit B from Σ21a (25°) GB, incorporating some additional green A units.

The atomic structure for Σ13b was anticipated to be similar to Σ21a and Σ7, however, contrary to expectations, it was found to be different. The observed discrepancy in the expected results of Σ13b may be attributed to various factors such as the effects of specimen thickness and the presence of different microstates. The presence of an additional atomic column could be attributed to the phenomenon of probe dechanneling [40], which is influenced by the orientation and thickness of the specimen. In thicker samples, dynamic scattering can cause the probe intensity to spread out beyond a single atomic column, affecting the adjacent columns and resulting in fluctuating contrast between

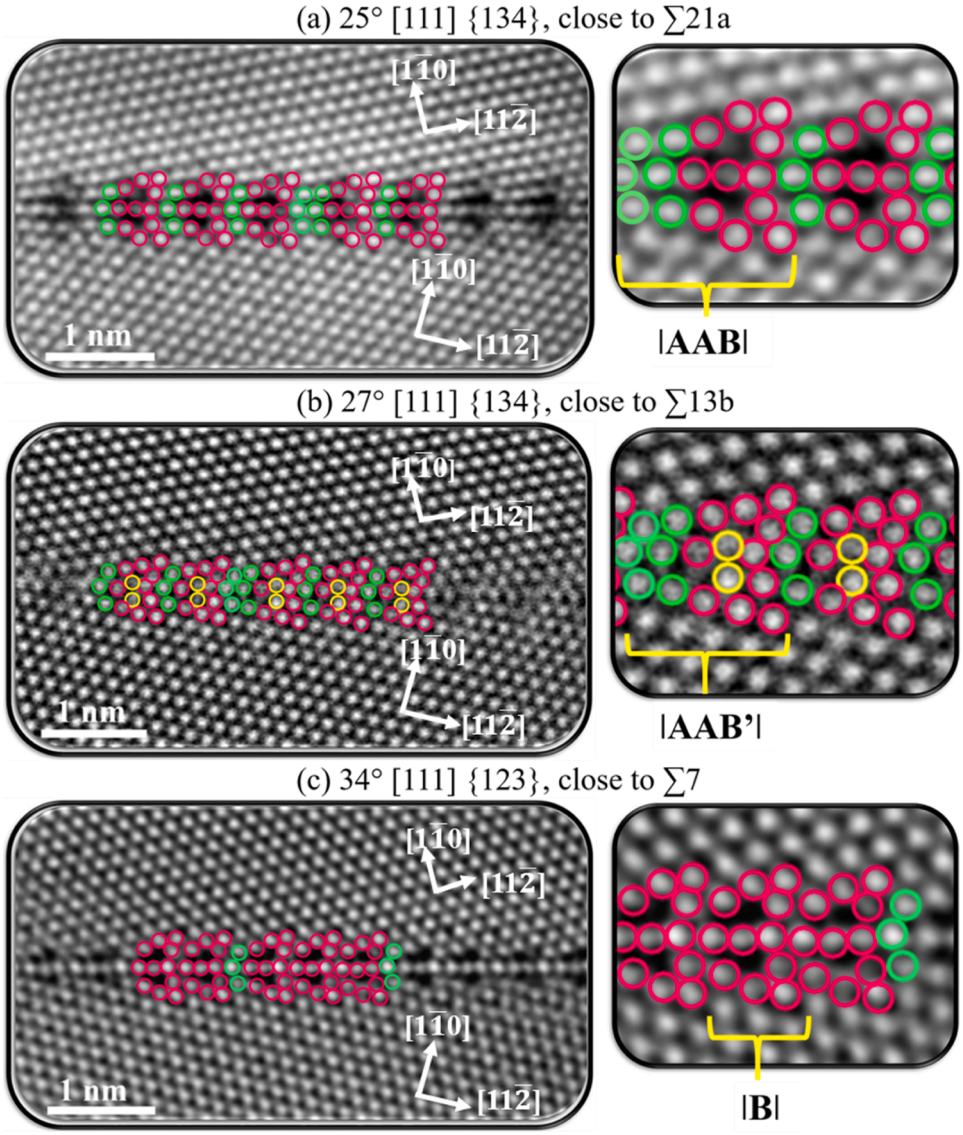

Fig. 2. STEM-HAADF images showing the atomic-resolution details of symmetric Σ21a, Σ13b and Σ7 GBs viewed along the [111] zone axis. Atomic structure of symmetric (a) Σ21a {134} (b) Σ13b {134} and (c) Σ7 {123}. The different color of the atomic columns serves to emphasize the structural units. The red and green color circles form the fundamental SUs (i.e. A and B) for each GB. Note that the GB planes reported here are approximate. (For interpretation of the references to colour in this figure legend, the reader is referred to the web version of this article.)

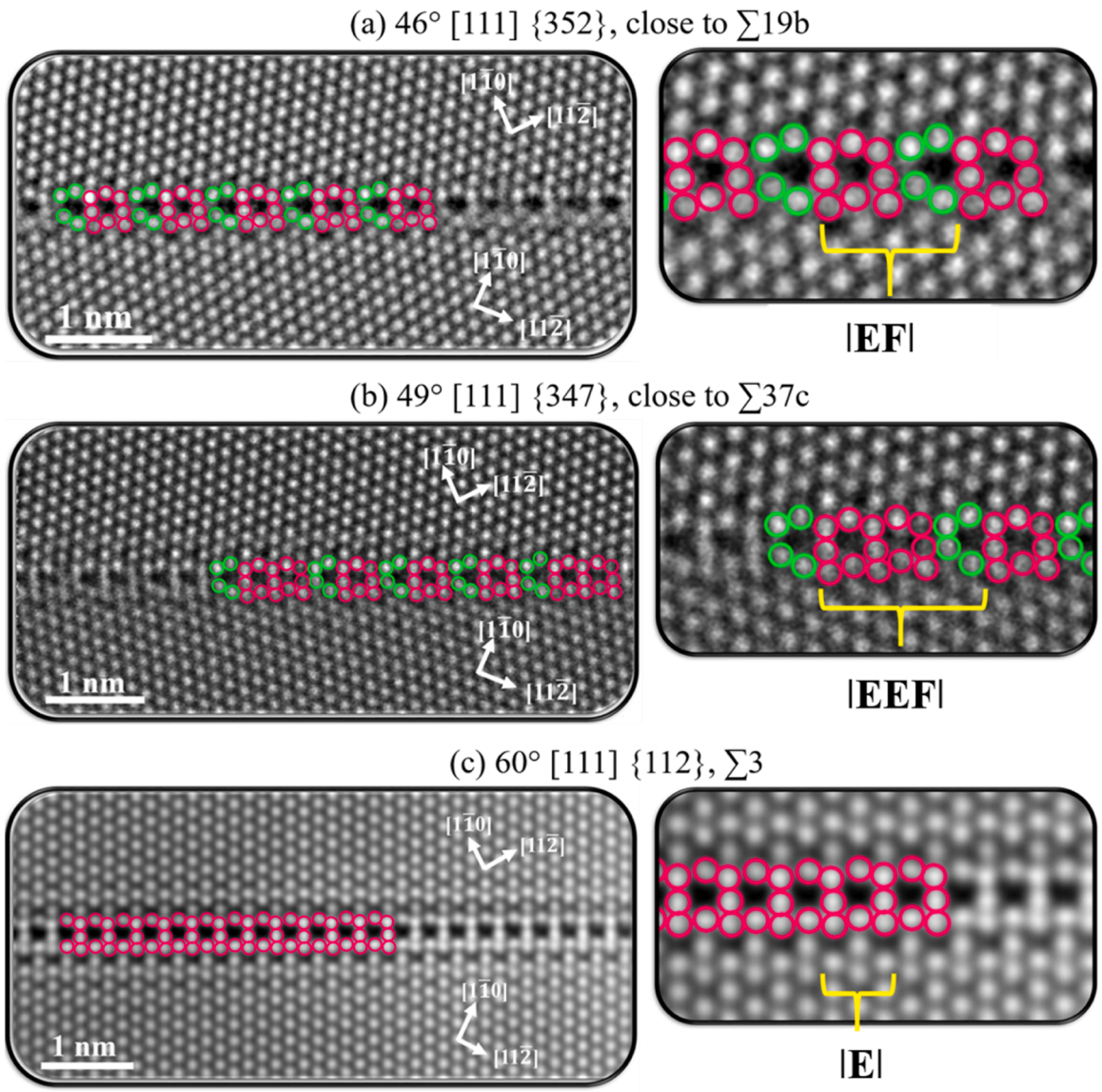

Fig. 3. STEM-HAADF images showing the atomic-resolution details of symmetric Σ19b, Σ37c and Σ3 GBs viewed along the [111] zone axis. Atomic structure of symmetric (a) Σ19b {352} (b) Σ37c {347} and (c) Σ3 {112}. The red and green color circles represent the square and trapezoidal shaped SUs (i.e. E and F). Note that the GB planes reported here are approximate. (For interpretation of the references to colour in this figure legend, the reader is referred to the web version of this article.)

Table 1
Type of [111] CSL boundaries, examined experimentally in S/TEM. The **Ideal θ** and **$\Delta\theta$** represent the CSL misorientation angle between the two grains and the allowable deviation from the exact CSL misorientation according to Brandon criterion, respectively. The Brandon criterion represents the allowable angular deviation ($\Delta\theta \leq 15\ \Sigma^{-1/2}$ degrees) from the exact coincidence [32]. The **Experimental θ** represents the measured value of the misorientation angle for various CSL boundaries investigated and shows that it slightly deviates from the **Ideal θ**. It should be noted that the measurement error for computing **Experimental θ** is within ± 0.5°.

[111] CSLs (Σ)	Ideal ($\theta \pm \Delta\theta$)	Experimental (θ)
Σ21a	21.8° ± 3.28°	24.8°
Σ13b	27.8° ± 4.16°	26.8°
Σ7	38.2° ± 5.67°	34.0°
Σ19b	46.6° ± 3.44°	46.0°
Σ37c	50.5° ± 2.47°	48.5°
Σ3	60.0° ± 8.67°	60.0°

them. Additionally, GBs have the ability to exhibit various microstates, which correspond to unique atomic arrangements and energetically favorable configurations. Similar to Σ3 GBs [28], it is plausible that Σ13b possesses multiple microstates and hence the structure differs. This will be further discussed after presenting the atomistically calculated structures of the boundaries.

The atomic resolution images of Σ19b (46°), Σ37c (49°), Σ3 (60°) are presented in Fig. 3 and their structures can be written as |EF|, |EEF| and |E|. The full atomic structure of the Σ19b is divided into two sub-units E and F, as highlighted by red and green circles in Fig. 3(a). The red sub-unit E exhibits a distorted square shape formed by 8 atomic columns, followed by the green sub-unit F, a trapezoid consisting of 4 atomic columns, as was observed also in Cu [27]. No other disruptions of this sequence at the symmetric segments are observed. The fundamental SU of Σ37c in Fig. 3 (b) consists of a contiguous double distorted square (13 atomic columns) E sub-unit, followed by a similar trapezoidal F sub-unit similar to Σ37c in Cu [41]. Moreover in Σ3, the red sub-unit E is observed to have an approximate square shape, comprising eight atomic columns, as also described in Ref. [28]. The spacing of the F units within the grain

boundary varies depending on the specific misorientation angle.

Additionally, it is noteworthy that the observed misorientation angle of the Σ37c boundary in Fig. 3b) is approximately 49°, which falls between the nominal misorientation angles of Σ19b (48.6°) and Σ37c (50.5°). This intermediate misorientation angle suggests the potential presence of a combination of the structures from both the ideal Σ19b and Σ37c, as observed in the experimental image. Here, the GB structures are termed as zipper structures by virtue of the analogy to the Σ19b {2 5 3} and Σ37c {3 4 7} GB structures in Cu [27,41], which will be further discussed later.

3.2. Atomistic simulation of symmetric variant I of Σ21a, Σ163, Σ67 and Σ7 GBs

So far, the experimentally observed structures are from GBs that deviate slightly (within the Brandon criterion) from the nominal CSL

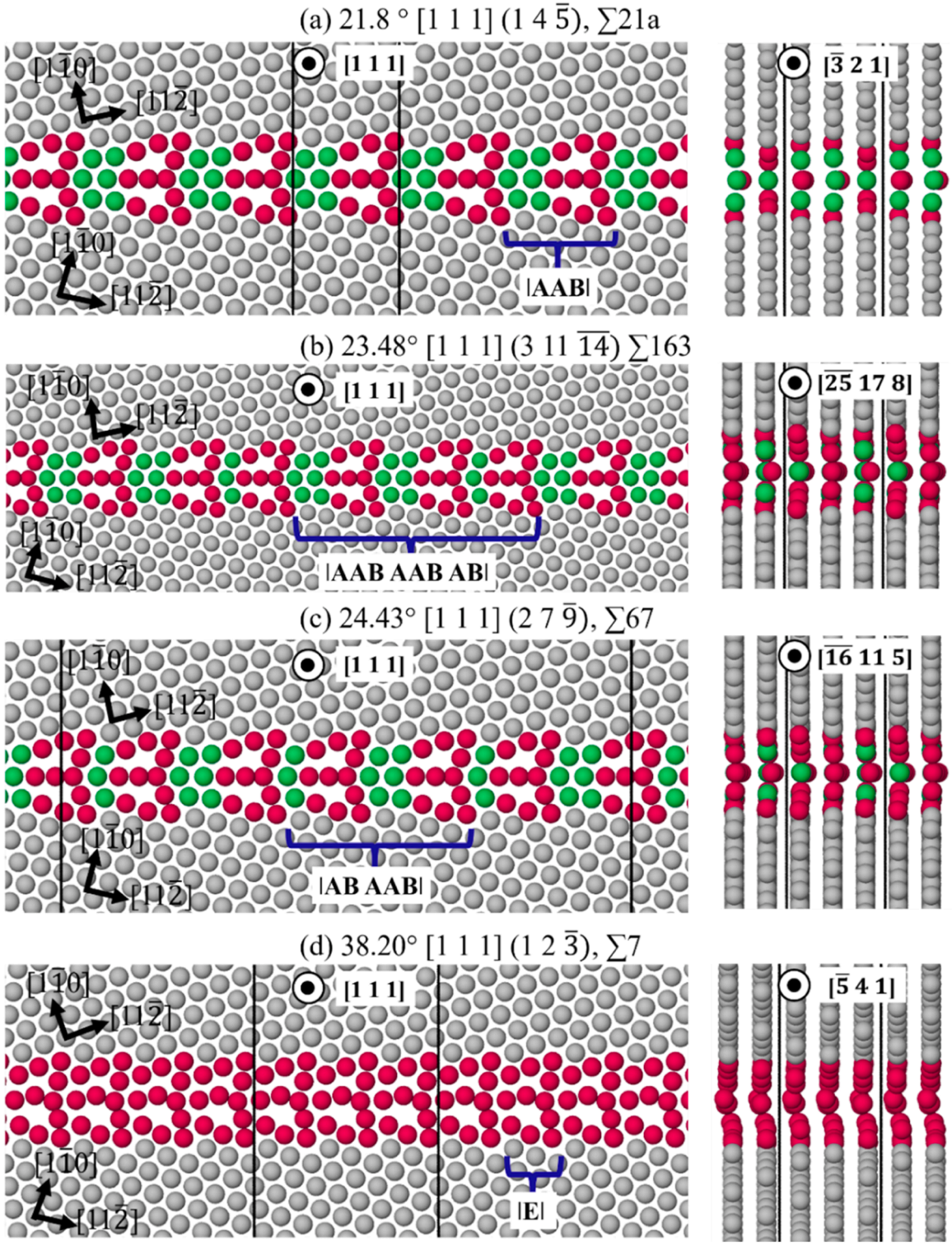

Fig. 4. Simulated atomic structures of the GBs (a) Σ21a (21.79°), (b) Σ163 (23.48°) (c) Σ67 (24.43°) GBs and (d) Σ7 (38.20°) GBs. The figure shows the atomic structures of the four GBs along the [111] tilt axis and z-axis (rotated by 90° around GB normal).

misorientation and the GB habit plane (see Table 1).

These small deviations influence GB structural units, which cannot be directly studied through experiments. Furthermore, experimental access to the 3D atomic structures and excess properties of GBs in this context is limited. Therefore, simulations play a crucial role in investigating these aspects.

Fig. 4 depicts the change in the atomic structures of the GBs (symmetric variant I) as a function of misorientation angle, specifically ranging from the exact Σ21a misorientation (21.8°) up to 38.2°. Simulations were conducted at 0 K without any external stress applied. Additionally, Fig. 5 presents interfacial excess properties depicted by blue data points. In the case of Σ21a (21.8°) the atomic structure comprises of the bow and arrow red SUs, identical to the observed experimental structural units (i.e. B units). In addition, the GB structure also embodies two A units consisting of three atomic columns (see Fig. 2(a)). Slight deviations from the misorientation angle result in the Σ163 (+1.7°) and Σ67 (+2.6°) GBs. These deviating GBs still exhibit alternating A and B units, but the SU pattern changes from |AAB| to |AABAABAB| to |ABAAB|, i.e., the number of intermediate A units separating the B units decreases slowly.

The experimental image (Fig. 2(a)) at a misorientation of 25° contains fewer A units than expected for Σ21a, exhibiting both AAB and AB SU patterns, which fits to the prediction from the simulations. This is connected to changes of the excess energy and volume (Fig. 5), highlighting that deviations from the exact misorientation even within the Brandon criterion are significant for structure and excess properties of GBs. When reaching the Σ7 GB at 38.2°, the A units disappear completely. The Σ7 is thus a delimiting GB. A comparison with the experiment, however, shows another discrepancy.

The Σ7 structure more closely resembles the zipper structure than the bow & arrow structure, which can be most clearly seen by looking at the center row of atoms in the red motifs. This center row is no longer a straight line, like in the bow & arrow structures of lower misorientations. This is connected with an offset $[B_1]$ between (111) planes, visible in the side views of (Fig. 4) and plotted in Fig. 5(c). Note that the structures with positive and negative values of $[B_1]$ are degenerate and we simply chose one sign convention here for plotting. In order to resolve this discrepancy, we heated several of the simulated GBs to 300

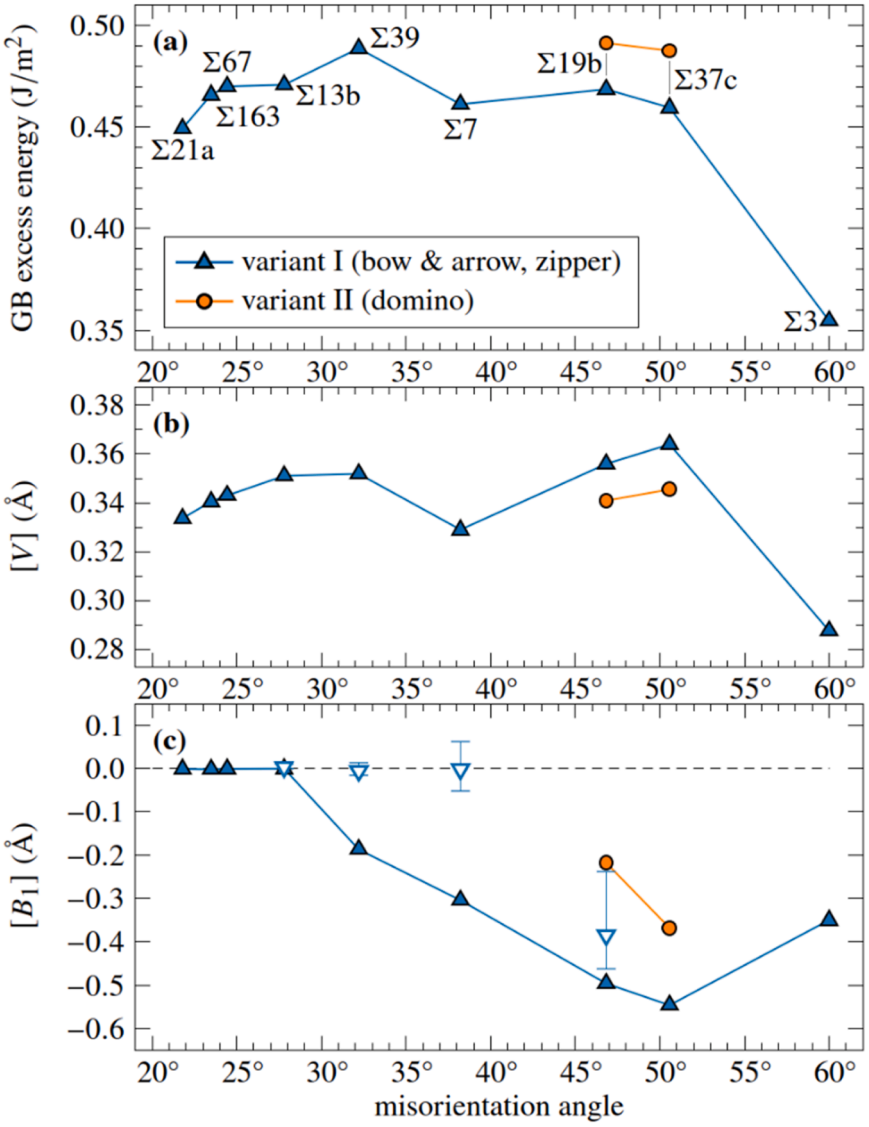

Fig. 5. Excess properties of the GB structures (starting from a misorientation angle of 21.8° up to 60°) as predicted by the computer simulation. (a), (b) and (c) represent the change in GB excess energy, excess volume [V] and excess shear [B_1] along the [111] tilt axis as a function of increasing misorientation angle. Solid symbols in the plot represent that the simulations were conducted at 0 K. The blue and orange data points, respectively, represent the excess properties of the symmetric variants I and II of the GBs. Empty blue symbols in c) corresponds to the [B_1] value at 300 K. (For interpretation of the references to colour in this figure legend, the reader is referred to the web version of this article.)

K and calculated their average $[B_1]$ (Fig. 5(c), open symbols). Since $\pm[B_1]$ are degenerate states, we discarded simulations where the structure fluctuated between these values during the simulation, meaning that the simulations with an averaged $[B_1] \approx 0$ do indeed contain distinct structures/microstates (see Fig. A- 1(b)) from those with $[B_1] \neq 0$. After this, the Σ13b GB still exhibited the bow & arrow structure, the Σ7 transformed to the bow & arrow structure, and the Σ19b still exhibited the zipper structure. More details on these structural differences are provided in the Appendix. These finite temperature observations are now in full agreement with the experimental observations at room temperature. Based on the observed results, the atomic structure of GBs can be categorized into two groups: those with $[B_1] \approx 0$, which exhibit bow and arrow structures in the projection (i.e. [111]), and those with $[B_1] \neq 0$, which display zipper-like structures. This transition is affected by the temperature.

3.3. Atomic structures of symmetric variants II of Σ19b, Σ37c and Σ3 GBs

The atomic structure of symmetric variants II of Σ19b {178} and Σ37c {189} shows a very distinct atomic structure with a change in GB inclination by 30°. The total GB structure of both the GBs is composed of a combination of the two inclined characteristic sub-units, as indicated by red circles (see Fig. 6(a) and (b)).

In Σ19b, the SU notation is |K K'|, where K represents the low inclined domino shaped unit (w.r.t the normal of the GB plane) while K' is the mirror image of the inclined sub-units (i.e. K) along the GB plane. Here, the structural units are referred to as domino structures due to their resemblance to the structures in Σ19b {1 7 8} and Σ37c {1 10 11} GBs in Cu [25–27]. The arrangement of two of these sub-units builds up the repetitive unit of the GB. The two subunits that make up the entire domino structure alternate between one low-inclined K and one mirrored K' unit. Similarly, the domino structure in Σ37c is |L L'|, where L represent the high inclined domino unit and L' are the mirrored L domino with respect to the GB plane.

The atomic structure of a Σ3 {110} comprises instead of {112} inclined facets of approximately 3.4 nm in length (see Fig. 7). These facets are expected to be present at room temperature according to previous findings in the Refs. [42–45], where similar faceting in Al and Au GBs was observed. However, the specific details regarding the Burgers vector and the atomic structure were previously unknown but have been investigated in this study. The atomic structure of these {112} facets consists of E square units as described above for the Σ3 {112} structure. We note that the K, L, and E structures share some similarities regarding the square units they consist of. This is investigated in more detail in Ref. [46].

Burgers circuits around single facet junctions have not been reported before. The most common method to obtain Burgers vectors of GB defects is due to Medlin et al. [47], where the GB crossings are chosen in such a way that their contributions to the Burgers vector cancel out. The rest of the circuit can then be expressed in terms of undistorted fcc crystal coordinates and the terms due to both half circuits in the separate crystallites can be added after transforming them into the same coordinate system. This is only possible if parallel GB facets are crossed and thus requires the inclusion of two facets [47]. Recently, Frolov et al. [48] proposed a method to compute the Burgers vector components due to unequal GB crossings using simulation data. This can be combined with Medlin et al.'s method for the rest of the circuit. Our analysis is shown in

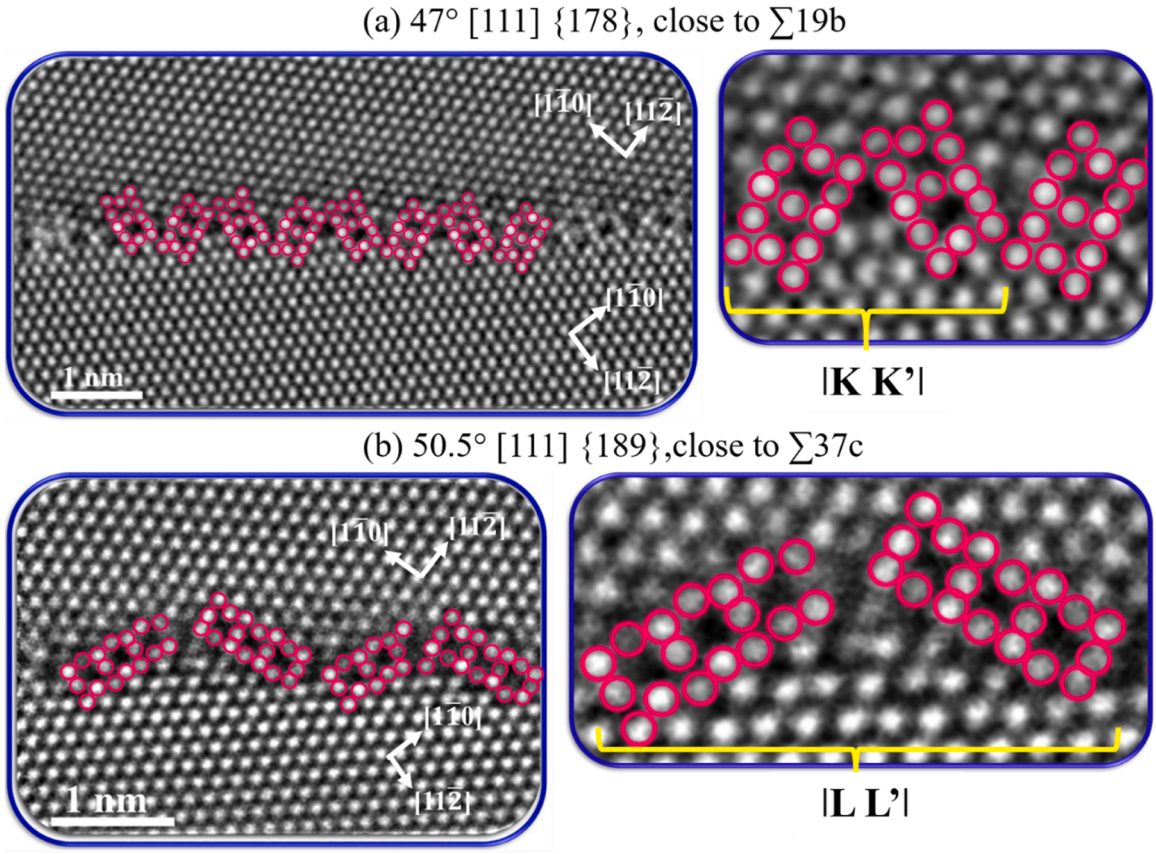

Fig. 6. STEM-HAADF images showing the atomic-resolution details of the symmetric variant II of Σ19b, Σ37c and Σ3 GBs viewed along the [111] zone axis. Here, the GB plane inclination is 30° w.r.t the GBs observed in Fig. 3. Atomic structure of symmetric (a) Σ19b {178} and (b) Σ37c {189}. The red color circles represent the inclined square shaped and trapezoidal shaped SUs while dark red color circles represent the mirrored structural units of the inclined units. (For interpretation of the references to colour in this figure legend, the reader is referred to the web version of this article.)

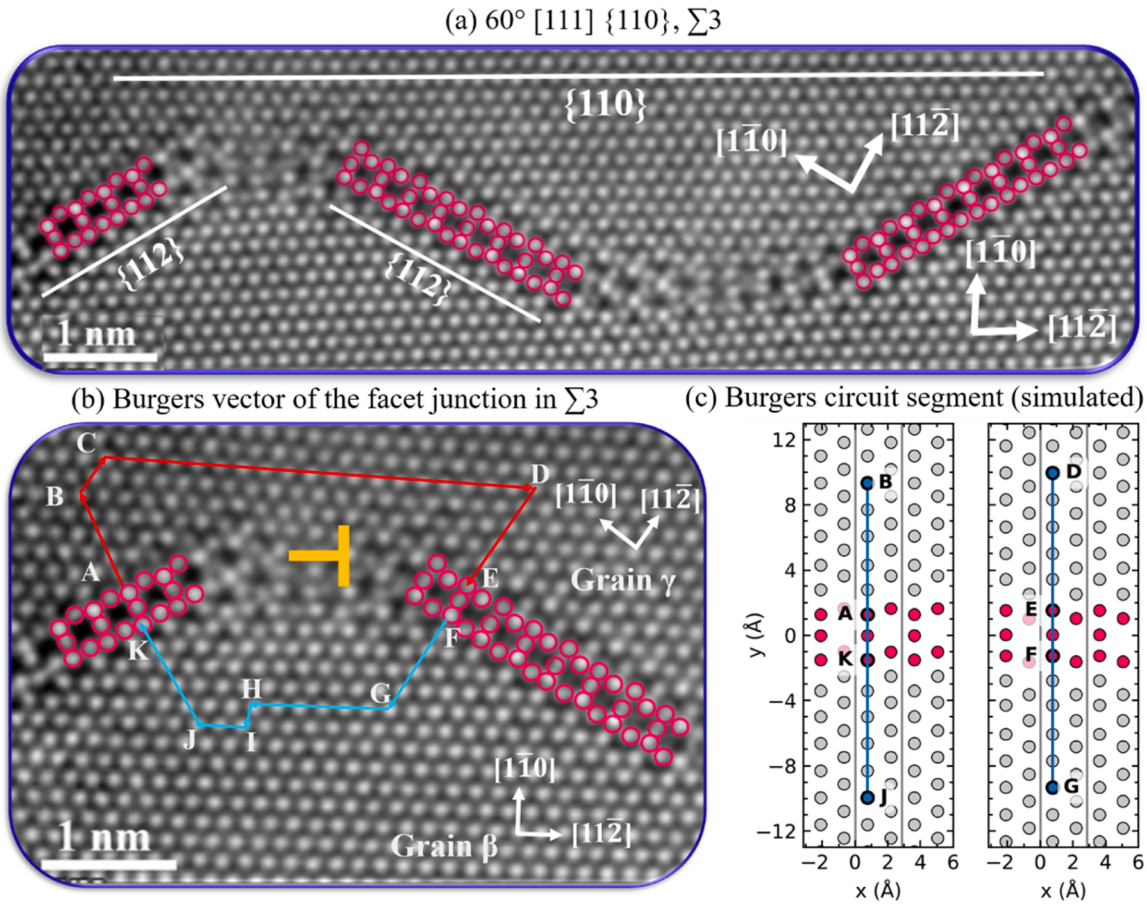

Fig. 7. STEM-HAADF images showing the atomic-resolution details of (a) symmetric Σ3 {110} grain boundary viewed along the [111] zone axis. Note that globally the GB plane is {110} but locally it is facetted into {112} planes. (b) depicts the full Burgers vector circuit around the facet junction and (c) corresponds to the segment of the Burgers circuit normal to GB plane in the simulated Σ3. The red color circles represent the inclined square shaped SUs and the mirrored structural units of the inclined squared units. A to E show the Burgers circuit in grain γ while F to K indicate the Burgers circuit in grain β. The calculation using Medlin et al.'s [47] and Frolov et al.'s [48] methods show that these facet junctions are associated to Burgers vector $b = a/2\ [01\bar{1}] + 5/3\ \boldsymbol{a}\ [1\bar{2}1]/6$. The letter a stands for the lattice parameter. (For interpretation of the references to colour in this figure legend, the reader is referred to the web version of this article.)

Fig. 7. For $\overline{DG}$ and $\overline{JB}$, we marked the same lines in undistorted/unfaceted Σ3 {112} GBs from the simulation and measured their distance in the system without a defect.

We used simulation data because the measurements from $T = 0$ K simulations contain 3D information and are accurate to the precision of the computation compared to the much larger measurement errors in experiment. Then we computed the two half circuits $\overline{BCD}$ and $\overline{GHIJ}$ using Medlin et al.'s method. We rotated the GB crossings by ±30°, transformed everything into the same coordinate system, and added the circuit. The result expressed in the coordinate system of the upper crystallite is a Burgers vector that is close to the [10$\bar{1}$] direction: $\boldsymbol{b} = a\ [0.278, 0.056, -0.222] = a/2\ [01\bar{1}] + 5/3\ a\ [1\bar{2}1]/6 = a/6\ ([11\bar{2}] - 2\ [\bar{2}11])\ /\ 3$. The vectors $a/2\ [01\bar{1}]$, $a\ [1\bar{2}1]/6$, $a/6\ [11\bar{2}]$, and $a/6\ [\bar{2}11]$ are DSC vectors. The Burgers vector of the present junction thus cannot be expressed as a sum of whole DSC vectors. Since the facets are not translationally equivalent, but contain an additional rotation, non-DSC vectors are allowed in the junction.

3.4. Atomistic simulations: comparison of symmetric variants of Σ37c GB

We have so far discovered from the experimental observation that the symmetric variant II of the same type of boundaries (Σ19b, Σ37c and Σ3) exhibits different atomic arrangement as a result of different atomic planes, compared to variant I.

To determine whether or not these different structures belonging to the same boundary type have different GB properties, we have simulated the atomic structures and the excess properties of two symmetric variants of Σ37c GB (with the habit plane of {3 4 7} and {1 10 11}, respectively) as illustrated in Fig. 8. Note that there are more variants for other GBs, as described in Ref [16].. The simulated atomic structure of Σ37c {3 4 7} GB exhibit a zipper kind of structure having two distorted square units, followed by a trapezoidal unit, in agreement with the experimental result above (see Fig. 3(b)). In contrast, the Σ37c {1 10 11} structure possesses a domino kind of structure, which is similar to the one mentioned in Ref [16]. . As indicated in Fig. 5, two distinct types of structures are found with differing thermodynamic excess properties (indicated by orange color data points). In addition, analyzing the cross-sectional view reveals different magnitudes of translation of {111} planes (i.e. $[B_1]$) across the GB with 0.55 Å and 0.37 Å for the zipper and domino structures, respectively. Comparable structures, such as domino and zipper, were also detected at the Σ19b boundary for {5 3 2} and {8 7 1} GB planes (please see Fig. A-2 in the appendix).

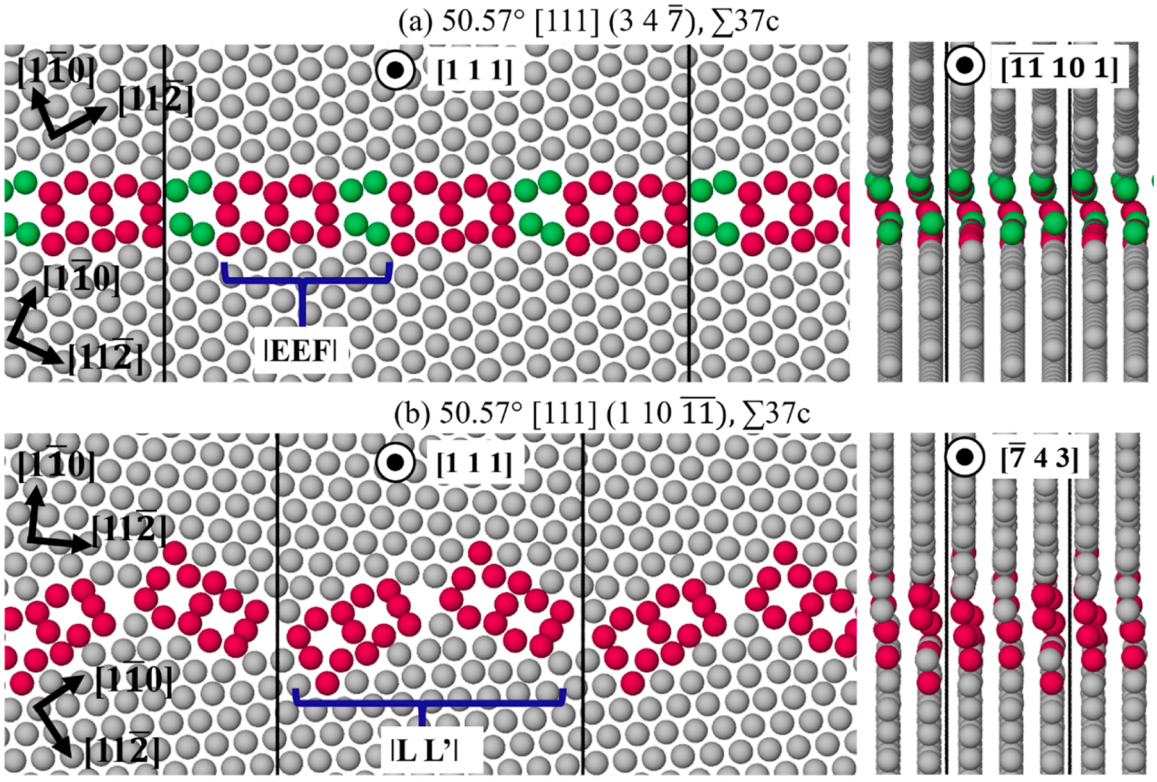

Fig. 8. Simulation of two symmetric variants of Σ37c GB. (a) Symmetric variant I: Σ37c {347} and (b) Symmetric variant II: Σ37c {1 10 11} GBs along the <111> tilt axis and the cross section. The simulation exhibits two different atomic structures corresponding to two different GB planes. The images on the right are rotated by 90° around the GB normal.

4. Discussion

4.1. Atomic structures of symmetric variant I of the GBs as a function of misorientation

This discussion delves into the intricate relationship between the misorientation angle, the GB plane, and the resulting variations observed in the atomic structure of [111] tilt GBs. Additionally, it aims to provide a comprehensive understanding by specifically examining the influence of atomic structures on excess properties. To date, there is a lack of experimental studies investigating the variations in atomic structure of [111] tilt GBs as a function of misorientation in pure fcc metals. However, three theoretical studies conducted by Frost et al. [17], Sutton et al. [15] and Wang et al. [12], as well as three experimental studies [25–27], have explored the structures of several [111] tilt GBs in pure Al and Cu. However, it is noteworthy that none of the proposed SUs by Frost et al., utilizing a hard sphere model [17], align with the observed experimental findings in this particular study. This hard sphere model, which employs rigid displacements without any internal relaxations, is too simplistic to predict the [111] tilt GBs' actual structures.

Interestingly, Sutton and colleagues [15] performed simulations on [111] tilt GBs (symmetric variant I) in Al with increasing misorientation and discovered a distinct, discontinuous change in the boundary structure between two delimiting GBs. They proposed the existence of two distinct groups of boundary structures characterized by $[B_1]$, which indicates a {111} plane translation along the cross section. Group I consists of GBs with $[B_1] \approx 0$, while group II comprises GBs with $[B_1] \neq$

Table 2
Simulation results from Sutton et al. [15], which shows the structure of symmetric variant I GBs with increasing misorientation angle. There are two groups of boundary structure depending on the value of $[B_1]$. The fundamental structural units of the boundaries in first and second group are A and B* and C, D, E and F units, respectively. For the GB structures, please refer to Ref. [15]. Note that two different microstates are observed for Σ21a and Σ13b GBs near the discontinuity.

GB categorization	GB type	θ	$[B_1]$	Structure
	Σ 57	13.17°	−0.017	|AAAAAB*|
	Σ 43	15.18°	−0.014	|AAAAB*. AAAAB*. AAAAB*|
Group I ($[B_1] \approx 0$)	**Σ 31a**	17.90°	−0.015	|AAAB*. AAAB*. AAAB*|
	Σ 21a	21.79°	−0.021	|AAB*|
	Σ 13b	27.80°	−0.020	|AB*. AB*. AB*|
	Σ 21a	21.79°	+0.264	|C|
	Σ 13b	27.80°	+0.274	|D. D. D|
Group II ($[B_1] \neq 0$)	**Σ 7**	38.21°	+0.283	|E. E. E|
	Σ 19b	46.83°	+0.277	|EF. EF. EF|
	Σ 37c	50.57°	+0.277	|EFF. EFF. EFF|
	Σ 3	60°	+0.235	|F|

0. Table 2 presents the detailed values of $[B_1]$ for each group explored in their study. The simulations based on Sutton's work do not match with our experimental observations. Later, Wang et al. [12] examined the structures of [111] GBs in Cu, accounting for the influence of possible metastable structures. Unlike Al [15], they found that the boundary structure changed continuously with increasing misorientation for Cu. When comparing the predicted structures in Cu [12] with the observed structures in Al (see Figs. 2, 3, and 10), some similarities were observed in the structural units. However, their atomic distances and angles differed due to material variations. Furthermore, no significant resemblances were found in the other simulations of Ref. [12]. The discrepancies in the simulations by Sutton and Wang may be due to the use of unphysical pair potentials [49]. Furthermore, the GBs in different materials can have different microstates, as was also observed in the case of Σ3 [111] in Al [28]. This may lead to the differing structure of the same boundary in different materials.

To validate these simulation findings from Refs. [12,15], we examined the evolution of atomic structures of six [111] tilt GBs with increasing misorientation angles using aberration-corrected S/TEM. The examined GBs included symmetric variant I of Σ21a, Σ13b, Σ7, Σ19b, Σ37c, and Σ3. In addition to the experimental analysis, we performed simulations to assess the translation of [111] planes and other excess properties. Notably, the investigated structures obtained in this study exhibited a similar trend in terms of $[B_1]$ to the older simulations [15]. However, upon comparing the structural units, we noted a lack of agreement between our observed structures (Fig. 10) and those proposed by Sutton et al. in Ref. [15] (see Fig. 9(a)). The good match, however, between the structures observed experimentally with those obtained in our simulations with more modern EAM potentials [33] means that we can be more confident in the qualitative structure predictions of the present simulations compared to the earlier work [12, 15]. Interestingly, we identified two distinct structural units of GBs based on different values of $[B_1]$ within specific misorientation ranges. Within the range of misorientation angles from $21^\circ \leq \theta \leq 34^\circ$, GBs (Σ21a, Σ13b, and Σ7) with $[B_1] \sim 0$ exhibited a distinctive "bow and arrow" structure (see Fig. 10). On the other hand, GBs (Σ19b, Σ37c, and Σ3) with $[B_1] \neq 0$ demonstrated a notable "zipper" structure for misorientation angles ranging from $46^\circ \leq \theta \leq 60^\circ$ (see Fig. 10(b)).

Additionally, insights into the influence of slight deviations in GB misorientation from the ideal one on various structural motifs and their interfacial properties have been obtained through simulations. Comparing the simulated and experimental boundary structures, our simulations predict the same trend as the experiment: a reduction in the prevalence of A type structural motifs as the misorientation deviates from the ideal parameters, leading to changes in the excess properties (see Fig. 5). In ceramics [50–52], the presence of additional structural units in near-Σ GBs has been linked to the existence of DSC dislocations, which could be related to the ionic bonding nature of the ceramic material. To our knowledge, such type of structural variations have not been observed in metallic materials. In these materials, DSC dislocations are frequently intricately associated with steps or disconnections within the GB [28,47]. Conversely, on conducting the Burgers circuit analyses around various parts of the GB, we observed that the presence or absence of structural motifs is not correlated with steps or clearly identifiable dislocations/disconnections on the near-Σ21a GB in Al.

It is noteworthy that even a minor alteration in misorientation can

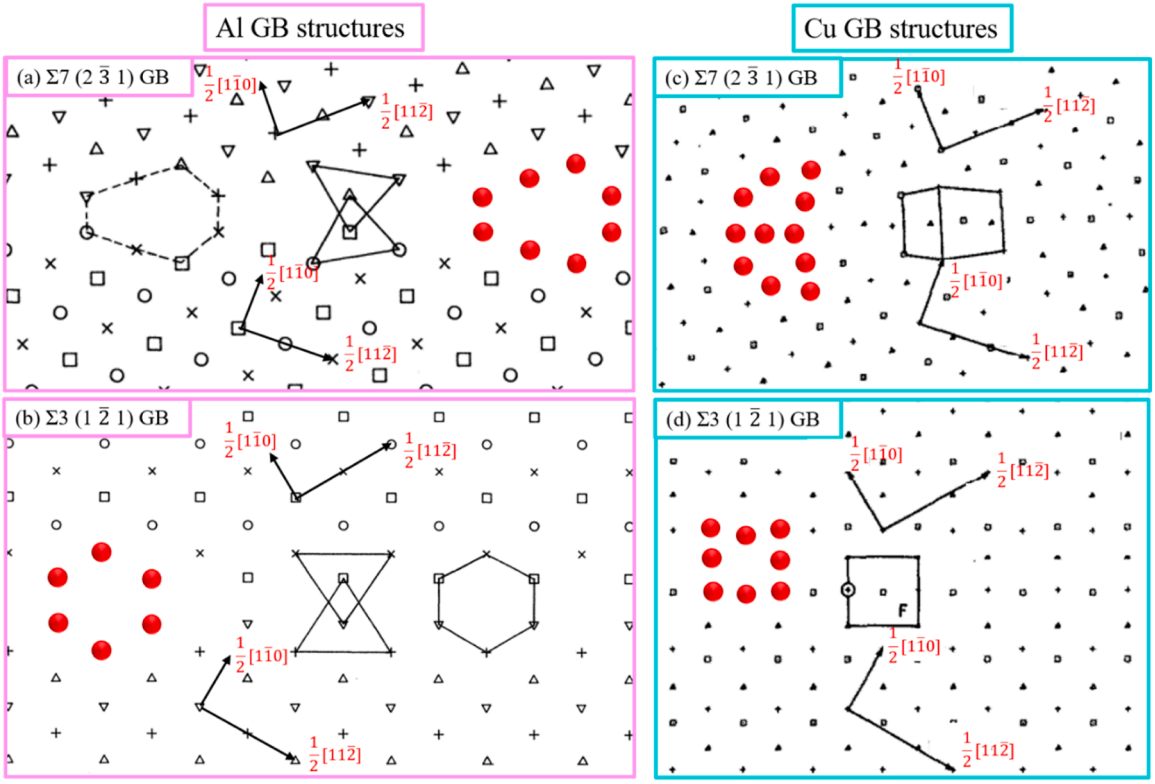

Fig. 9. Theoretical structures of Σ7 and Σ3 GBs along [111] tilt axis from literature [12],[15]. At the GBs, the red circles form repeating SUs. (a) and (b) show the SUs of Σ7 and Σ3 in Al from Sutton et al. [15]. (c) and (d) show the SUs of the same GBs in Cu from Wang et al. [12]. The figure clearly depicts that the structures look different in both theoretical studies. (For interpretation of the references to colour in this figure legend, the reader is referred to the web version of this article.)

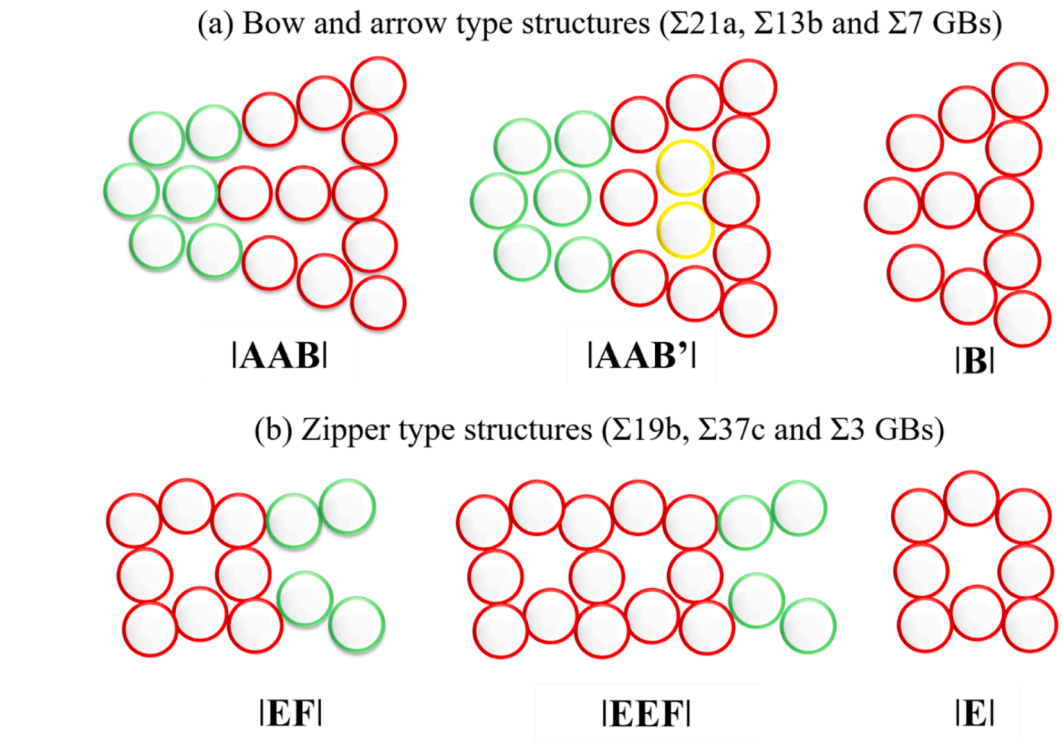

Fig. 10. Schematics illustration of the atomic structures for different GBs as a function of misorientation angle and GB planes as found by STEM studies in this work. (a) and (b) represent the SUs of Σ21a, Σ13b and Σ7 GBs (from left to right) as a function of misorientation (symmetric variant I).

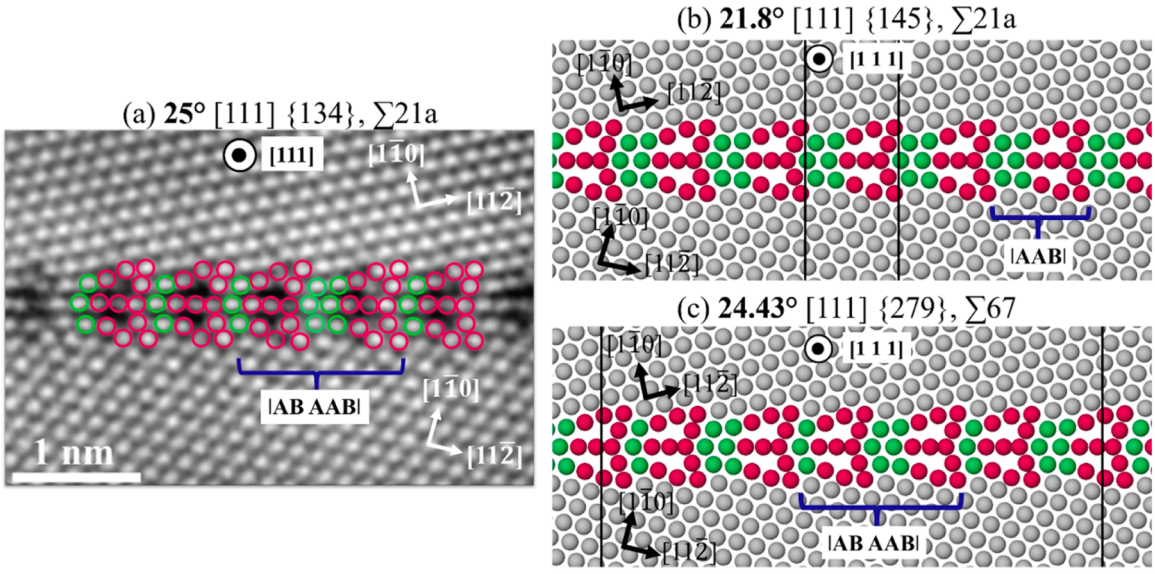

Fig. 11. Comparison of the experimental and simulated structure of Σ21 GB. (a) shows the experimental structure of Σ21 boundary which is more similar to Σ67 GB, displayed in (c). The Σ67 boundary has a misorientation deviation of around 2° from the ideal Σ21 GB (as shown in b)). For every 3 B type units, the ideal Σ21 boundary has 6 A type units while number of A units in Σ67 boundary is lower than 6.

have a considerable effect on the excess properties of GBs. For instance, let us consider the case of a Σ21 GB, where the experimental misorientation is approximately 25°. This value is closer to that of a Σ67 GB rather than the ideal Σ21 GB (please see Fig. 11(a)–(c)). Interestingly, despite having a small deviation, the GB energy of Σ67 GB is higher than the ideal Σ21 boundary (see Fig. 5). Though this small deviation in misorientation may not sound big and can be easily overlooked in EBSD measurements, it can play a significant role in influencing GB related phenomena like microstructural evolution, GB migration and thermodynamic driving force for the segregation of solute elements at the GBs

in a polycrystalline Al. Specifically, GBs with higher energy are more prone to solute element segregation than those with lower energy [41, 53]. In addition, GB energy also plays an important role in controlling other properties such as diffusion and mobility. Furthermore, it is often found that higher energy GBs are more prone to structural transitions, that eventually impact the mobility of the GBs and control the grain growth in the material [54,55]. Therefore, the GBs like Σ21a (21.8°) and Σ67 (24.4°) GBs observed in the current study may respond differently towards segregation and grain growth phenomena in reality.

4.2. Atomic structures of symmetric variant II of the GBs

The discovery of differing properties and behavior among GBs with distinct misorientations and GB planes [14,27] has prompted further investigation into the atomic structure of symmetric variant II of Σ19b, Σ37c, and Σ3 GBs. These GBs share the same grain misorientation but possess different GB planes (30° rotated). Notably, there is a dearth of theoretical or experimental studies concerning the atomic structures of symmetric variants of the [111] tilt GBs, except for the Σ19b and Σ37c GBs in copper, as explored by Meiners et al. [25,27] and Langenohl et al. [26,41]. Meiners et al. [27] discovered two distinct atomic structures for the Σ19b GBs in copper, namely the zipper structure for the {253} plane and the pearl structure for the {187} plane. Moreover, an additional metastable GB structure, referred to as the domino phase, was observed for Σ19b {187} GB [25]. Each of these phases has distinct excess properties and can be transformed into the other.

The investigation of the two symmetric variants of Σ19b and Σ37c GBs in Al revealed contrasting structures: the Σ19b {352} GB displayed a zipper-like structure resembling Cu, while the Σ19b {187} GB exhibited a stable domino structure instead of the expected pearl structure observed in Cu. Despite examining five lamellas with Σ19b {187} GB in Al, no pearl phase was observed in our Al samples. This suggests that the pearl phase in Al may have higher energy and be metastable compared to the domino phase. Simulations ($T = 0$ K) [16] have often predicted the pearl phase as the stable phase, however, in the case of Al, both the pearl and domino phases exhibit very similar GB energies. Nonetheless, our experimental results suggest that there is a noticeable deviation from the predicted closeness between the two phases in reality, highlighting the significance of validating simulations through experimental structures. Regarding Σ37c GBs, the Σ37c {437} GB exhibited a zipper-like structure, while Σ37c {189} GB displayed a stable domino structure in Al similar to Cu [26]. However, in contrast to Cu, the presence of a pearl phase was also not observed at Σ37c {189} GB in Al [26], consistent with the predictions from simulations [16]. In all cases where structures could be compared to those observed in Cu (except pearl), they were found to coincide between Al and Cu, despite their different lattice parameters, atomic bonding, and stacking fault energies. This indicates the occurrence of such structures more generically in fcc materials. Furthermore, the two different structures within each boundary (Σ19b and Σ37c) not only differed in atomic arrangement but also had distinct excess properties. The zipper structure had a lower grain boundary energy by 6 % compared to the domino structure for Σ37c GB, which may lead to different behavior for variant I and II.

5. Conclusion

In conclusion, this paper presents a comprehensive investigation into the atomic structure of [111] high-angle tilt GBs in Al and explores the relationship between their crystallographic parameters and GB excess properties. The study employs aberration-corrected high-resolution electron microscopy and atomistic simulations to analyze the atomic structures of multiple GBs with increasing misorientation angles. The results reveal the existence of two distinct groups of GBs, characterized by their misorientation range and the translation of {111} planes across the GB. These two groups exhibit different atomic structures referred to as "bow and arrow" and "zipper" structures. The study further demonstrates that deviations from the exact misorientation and inclination of the GB plane are directly associated with the change in structural units at the GB, although the CSL boundary type remains unchanged. However, atoms within the GB do exhibit sensitivity to such deviations, which is effectively examined through simulations. Recognizing the limitations of potential approximations in simulations, the paper emphasizes the significance of validating the simulation results with direct experimental structures. This ensures a more accurate representation of the GB properties.

Additionally, the study highlights the impact of different habit planes on the behavior of symmetric segments within the same GB type. The research findings reveal the presence of “domino” structures when there is a change in plane inclination by 30°. This discovery indicates that different SUs need to be considered for varying plane inclinations. Moreover, the study highlights that the inclination has a greater impact on the structure compared to the misorientation within the GB.

Further investigations analyzing the response of these GBs to stress and temperature variations will contribute to a deeper understanding of their real behavior and potential applications. Although tailoring these structures is still a challenge, this research provides valuable insights for future advancements in GB engineering.

Declaration of competing interest

The authors declare that they have no known competing financial interests or personal relationships that could have appeared to influence the work reported in this paper.

Data availability

The main datasets of this study are published at https://doi.org/10.5281/zenodo.10491520 Other data supporting the findings of this study are available from the authors upon reasonable request.

Acknowledgments

This project has received funding from the European Research Council (ERC) under the European Union’s Horizon 2020 research and innovation programme (Grant agreement No. 787446; GB-CORRELATE).

Appendix A

The 3D information contained in the atomistic simulations allows us to study the differences between the bow & arrow structures and the zipper structures in more detail. Fig. A1 shows the motifs of the Σ13b, Σ7, and Σ37c GBs. The motifs are very similar in all of them and we indicated both the way we marked the bow & arrow structure, as well as the squares from the zipper structure.

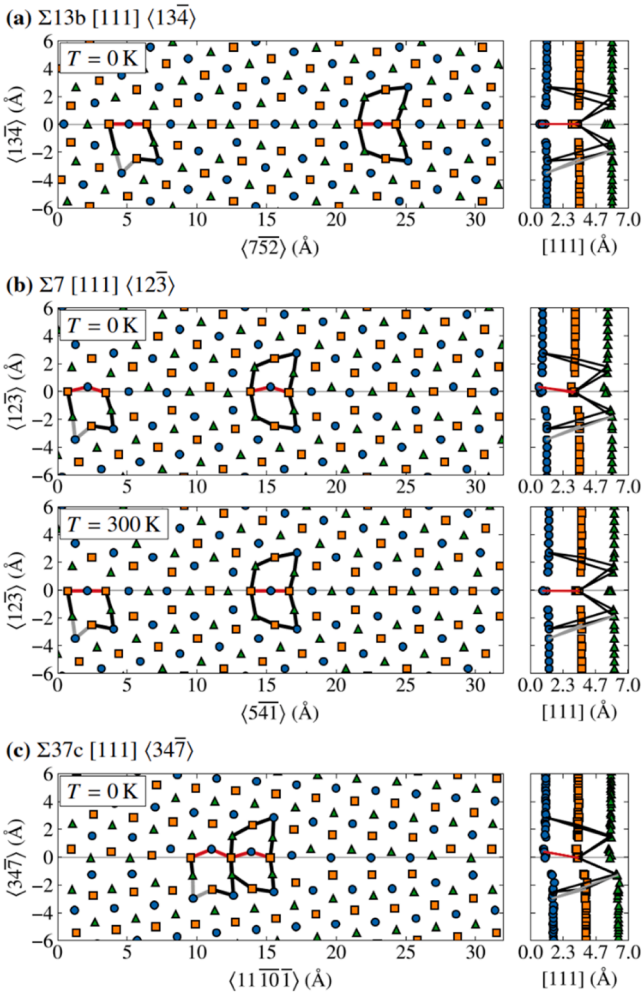

Fig. A1. Bow & arrow as well as zipper structures from atomistic simulations. The colors of the symbols indicate the ABC stacking of the (111) planes, as visible in the right column. The bow & arrow "B" structures and the zipper "E" squares are marked by lines. Black and red lines are shared between motifs, grey lines only belong to the "E" motif. It seems that the motifs apply to all structures, however, the difference lies in the atomic columns at $y = 0$ (red lines in the motif). For the bow & arrow structures, they lie on a straight line, as seen for Σ13b in (a). Here, there is also no offset between (111) planes. (b) The Σ7 GB exhibits the zipper structure at 0 K, indicated by deviations from the straight line and offsets between the (111) planes. At 300 K, the Σ7 GB has the bow & arrow structure as in experiment. (c) At higher misorientation, such as this Σ37c, we always find the zipper structure at all temperatures. (For interpretation of the references to colour in this figure legend, the reader is referred to the web version of this article.)

The difference between the structures becomes visible by considering the horizontal row of atoms at $y = 0$, or the sideview. For the bow & arrow structures, the center row is a straight line and the (111) planes are aligned. For zipper, the (111) planes have an offset leading the asymmetry in the $y = 0$ row. The Σ7 GB is a special case that exhibits a zipper structure at $T = 0$ K, but a bow & arrow structure at room temperature as observed in experiment. The room temperature shown in is the result of averaging the atomic positions over 250 ps in an equilibrated MD simulation (see also Methods).

Appendix B

Fig. A2(a) illustrates a zipper structure for symmetric variant I, whereas in Fig. A2(b), it depicts a domino structure for symmetric variant II. This observation aligns with what was discovered for the Σ37c GB configuration.

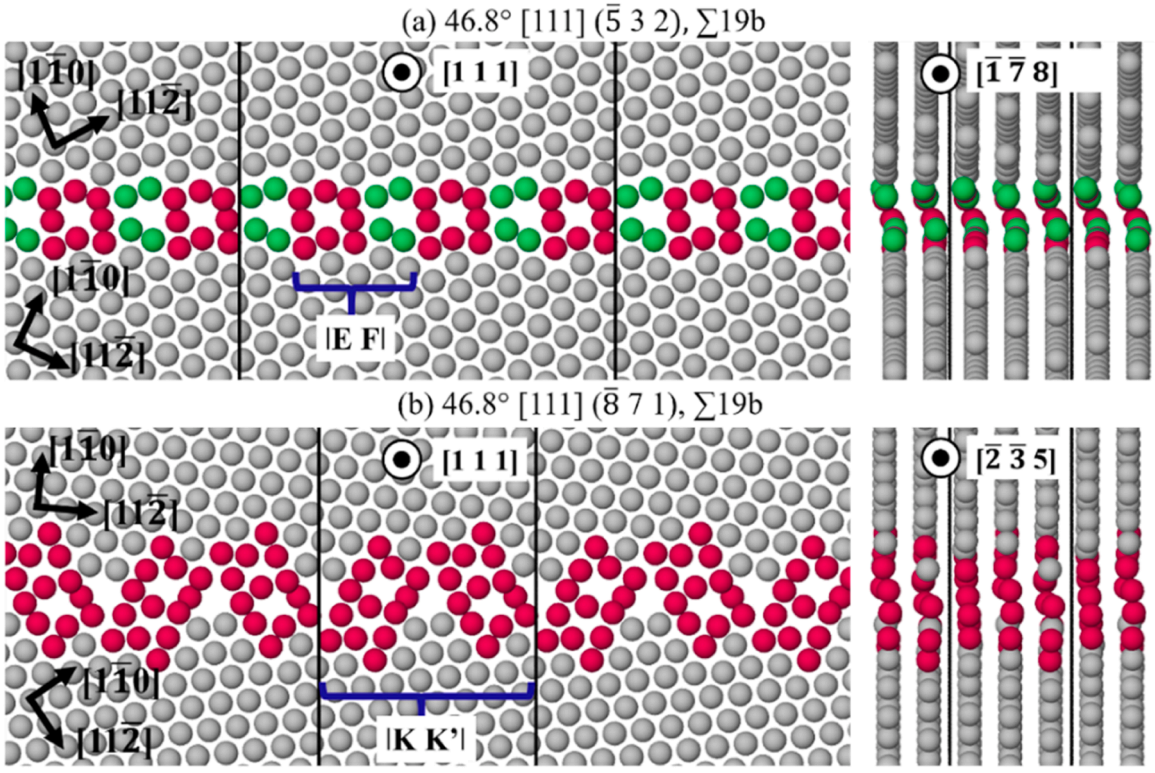

Fig. A2. Simulation of two symmetric variants of Σ19b GB. (a) Symmetric variant I: Σ19b {5 3 2} and (b) Symmetric variant II: Σ19b {8 7 1} GBs along the <111> tilt axis and the cross section. The simulation exhibits two different atomic structures corresponding to two different GB planes. The images on the right are rotated by 90° around the GB normal.

References

[1] L. Priester, Atomic Order of Grain Boundaries, Springer Science & Business Media, 2013, https://doi.org/10.1007/978-94-007-4969-6_3.

[2] S.V. Divinski, H. Edelhoff, S. Prokofjev, Diffusion and segregation of silver in copper Σ5(310) grain boundary, Phys. Rev. B Condens. Matter Mater. Phys. 85 (2012) 1–10, https://doi.org/10.1103/PhysRevB.85.144104.

[3] S.J. Dillon, M. Tang, W.C. Carter, M.P. Harmer, Complexion: a new concept for kinetic engineering in materials science, Acta Mater. 55 (2007) 6208–6218, https://doi.org/10.1016/j.actamat.2007.07.029.

[4] G. Duscher, M.F. Chisholm, U. Alber, M. Rühle, Bismuth-induced embrittlement of copper grain boundaries, Nat. Mater. 3 (2004) 621–626, https://doi.org/10.1038/nmat1191.

[5] P.R. Cantwell, T. Frolov, T.J. Rupert, A.R. Krause, C.J. Marvel, G.S. Rohrer, J. M. Rickman, M.P. Harmer, Grain boundary complexion transitions, Annu. Rev. Mater. Res. 50 (2020) 465–492, https://doi.org/10.1146/annurev-matsci-081619-114055.

[6] P.R. Cantwell, M. Tang, S.J. Dillon, J. Luo, G.S. Rohrer, M.P. Harmer, Grain boundary complexions, Acta Mater. 62 (2014) 1–48, https://doi.org/10.1016/j.actamat.2013.07.037.

[7] E.W. Hart, Two-dimensional phase transformation in grain boundaries, Scr. Metall. 2 (1968) 179–182, https://doi.org/10.1016/0036-9748(68)90222-6.

[8] J.W. Cahn, Transitions and phase equilibria among grain boundary structures, J. Phys. (Paris), Colloq. 43 (1982) 199–213, https://doi.org/10.1051/jphyscol:1982619.

[9] T. Frolov, D.L. Olmsted, M. Asta, Y. Mishin, Structural phase transformations in metallic grain boundaries, Nat. Commun. 4 (2013) 1–7, https://doi.org/10.1038/ncomms2919.

[10] T. Frolov, S.V. Divinski, M. Asta, Y. Mishin, Effect of interface phase transformations on diffusion and segregation in high-angle grain boundaries, Phys. Rev. Lett. 110 (2013) 1–5, https://doi.org/10.1103/PhysRevLett.110.255502.

[11] R.W. Balluffi, A.P. Sutton, Why should we be interested in the atomic structure of interfaces? Mater. Sci. Forum. 207–209 (1996) 1–12, https://doi.org/10.4028/www.scientific.net/msf.207-209.1.

[12] G.J. Wang, A.P. Sutton, V. Vitek, A computer simulation study of ⟨001⟩ and ⟨111⟩ tilt boundaries: the multiplicity of structures, Acta Metall. 32 (1984) 1093–1104, https://doi.org/10.1016/0001-6160(84)90013-0.

[13] J. Han, V. Vitek, D.J. Srolovitz, The grain-boundary structural unit model redux, Acta Mater. 133 (2017) 186–199, https://doi.org/10.1016/j.actamat.2017.05.002.

[14] M.A. Tschopp, S.P. Coleman, D.L. McDowell, Symmetric and asymmetric tilt grain boundary structure and energy in Cu and Al (and transferability to other fcc metals), Integr. Mater. Manuf. Innov. 4 (2015) 176–189, https://doi.org/10.1186/s40192-015-0040-1.

[15] A.P. Sutton, V. Vitek, On the structure of the structures of tilt grain boundaries in cubic metals: symmetric tilt boundaries. Series A, Mathematical and Physical Sciences 309, Philosophical Transactions of the Royal Society of London, 1983, pp. 1–36. https://doi.org/10.1098/rsta.1983.0020.

[16] T. Brink, L. Langenohl, H. Bishara, G. Dehm, Universality of grain boundary phases in fcc metals: case study on high-angle [111]symmetric tilt grain boundaries, Phys. Rev. B (2023) 107, https://doi.org/10.1103/PhysRevB.107.054103.

[17] Frost, H.J., Ashby, M.F., Spaepen, F., A catalogue of [100], [110] and [111] symmetric tilt boundaries in face-centered cubic hard sphere crystals, (1982), doi: http://nrs.harvard.edu/urn-3:HUL.InstRepos:13851353.

[18] D.L. Olmsted, S.M. Foiles, E.A. Holm, Survey of computed grain boundary properties in face-centered cubic metals: I. Grain boundary energy, Acta Mater. 57 (2009) 3694–3703, https://doi.org/10.1016/j.actamat.2009.04.007.

[19] E.R. Homer, G.L.W. Hart, C. Braxton Owens, D.M. Hensley, J.C. Spendlove, L. H. Serafin, Examination of computed aluminum grain boundary structures and energies that span the 5D space of crystallographic character, Acta Mater. 234 (2022) 118006, https://doi.org/10.1016/j.actamat.2022.118006.

[20] M. Schaffer, B. Schaffer, Q. Ramasse, Sample preparation for atomic-resolution STEM at low voltages by FIB, Ultramicroscopy 114 (2012) 62–71, https://doi.org/10.1016/j.ultramic.2012.01.005.

[21] J.M. Pénisson, U. Dahmen, M.J. Mills, Hrem study of a $\hat{1} = 3(112)$ twin boundary in aluminium, Philos. Mag. Lett. 64 (1991) 277–283, https://doi.org/10.1080/09500839108214622.

[22] M.J. Mills, M.S. Daw, G.J. Thomas, F. Cosandey, High-resolution transmission electron microscopy of grain boundaries in aluminum and correlation with atomistic calculations, Ultramicroscopy 40 (1992) 247–257, https://doi.org/10.1016/0304-3991(92)90121-Y.

[23] N. Sakaguchi, H. Ichinose, S. Watanabe, Atomic structure of faceted ∑3 CSL grain boundary in silicon: HRTEM and *ab-initio* calculation, Mater. Trans. 48 (2007) 2585–2589, https://doi.org/10.2320/matertrans.MD200706.

[24] W. Krakow, Structural multiplicity observed at a $\Sigma = 5/[001]53{\cdot}1^\circ$ tilt boundary in gold, Philos. Mag. A Phys. Condens. Matter, Struct. Defects Mech. Prop. 63 (1991) 233–240, https://doi.org/10.1080/01418619108204847.

[25] T. Meiners, T. Frolov, R.E. Rudd, G. Dehm, C.H. Liebscher, Observations of grain-boundary phase transformations in an elemental metal, Nature 579 (2020) 375–378, https://doi.org/10.1038/s41586-020-2082-6.

[26] L. Frommeyer, T. Brink, R. Freitas, T. Frolov, G. Dehm, C.H. Liebscher, Dual phase patterning during a congruent grain boundary phase transition in elemental copper, Nat. Commun. 13 (2022) 1–11, https://doi.org/10.1038/s41467-022-30922-3.

[27] T. Meiners, J.M. Duarte, G. Richter, G. Dehm, C.H. Liebscher, Tantalum and zirconium induced structural transitions at complex [111]tilt grain boundaries in copper, Acta Mater. 190 (2020) 93–104, https://doi.org/10.1016/j.actamat.2020.02.064.
[28] S. Ahmad, T. Brink, C.H. Liebscher, G. Dehm, Microstates and defects of incoherent Σ3 [111]twin boundaries in aluminum, Acta Mater. 243 (2023) 118499, https://doi.org/10.1016/j.actamat.2022.118499.
[29] C.M. Barr, E.Y. Chen, J.E. Nathaniel, P. Lu, D.P. Adams, R. Dingreville, B.L. Boyce, K. Hattar, D.L. Medlin, Irradiation-induced grain boundary facet motion: *in situ* observations and atomic-scale mechanisms, Sci. Adv. 8 (2022) 1–14, https://doi.org/10.1126/sciadv.abn0900.
[30] I. Adlakha, M.A. Bhatia, M.A. Tschopp, K.N. Solanki, Atomic scale investigation of grain boundary structure role on intergranular deformation in aluminium, Philos. Mag. 94 (2014) 3445–3466, https://doi.org/10.1080/14786435.2014.961585.
[31] M.L. Kronberg, F.H. Wilson, Secondary recrystallization in copper, JOM 1 (1949) 501–514, https://doi.org/10.1007/bf03398387.
[32] D.G. Brandon, The structure of high-angle grain boundaries in aluminium, Phys. Status Solidi. 31 (1969) 193–201, https://doi.org/10.1002/pssb.19690310123.
[33] Y. Mishin, D. Farkas, M.J. Mehl, D.A. Papaconstantopoulos, Interatomic potentials for monoatomic metals from experimental data and *ab initio* calculations, Phys. Rev. B Condens. Matter Mater. Phys. 59 (1999) 3393–3407, https://doi.org/10.1103/PhysRevB.59.3393.
[34] S. Plimpton, Fast parallel algorithms for short-range molecular dynamics, J. Comput. Phys. 117 (1995) 1–19, https://doi.org/10.1006/jcph.1995.1039.
[35] A.P. Thompson, H.M. Aktulga, R. Berger, D.S. Bolintineanu, W.M. Brown, P. S. Crozier, P.J. in 't Veld, A. Kohlmeyer, S.G. Moore, T.D. Nguyen, R. Shan, M. J. Stevens, J. Tranchida, C. Trott, S.J. Plimpton, LAMMPS - a flexible simulation tool for particle-based materials modeling at the atomic, meso, and continuum scales, Comput. Phys. Commun. 271 (2022) 108171, https://doi.org/10.1016/j.cpc.2021.108171.
[36] R. Hadian, B. Grabowski, J. Neugebauer, GB code: a grain boundary generation code, J. Open Source Softw. 3 (2018) 900, https://doi.org/10.21105/joss.00900.
[37] T. Frolov, Y. Mishin, Thermodynamics of coherent interfaces under mechanical stresses. I. Theory, Phys. Rev. B Condens. Matter Mater. Phys. 85 (2012) 12–15, https://doi.org/10.1103/PhysRevB.85.224106.
[38] T. Frolov, Y. Mishin, Thermodynamics of coherent interfaces under mechanical stresses. II. Application to atomistic simulation of grain boundaries, Phys. Rev. B Condens. Matter Mater. Phys. (2012) 85, https://doi.org/10.1103/PhysRevB.85.224107.
[39] G.H. Bishop, B. Chalmers, A coincidence - Ledge - Dislocation description of grain boundaries, Scr. Metall. 2 (1968) 133–139, https://doi.org/10.1016/0036-9748(68)90085-9.
[40] J. Liu, L.F. Allard, Surface channeling in aberration-corrected scanning transmission electron microscopy of nanostructures, Microsc. Microanal. 16 (2010) 425–433, https://doi.org/10.1017/S1431927610000450.
[41] L. Langenohl, T. Brink, G. Richter, G. Dehm, C.H. Liebscher, Atomic resolution observations of silver segregation in a [111]tilt grain boundary in copper, Phys. Rev. B 134112 (2023) 1–14, https://doi.org/10.1103/PhysRevB.107.134112.
[42] Z.X. Wu, Y.W. Zhang, D.J. Srolovitz, Grain boundary finite length faceting, Acta Mater. 57 (2009) 4278–4287, https://doi.org/10.1016/j.actamat.2009.05.026.
[43] T.E. Hsieh, R.W. Balluffi, Observations of roughening/de-faceting phase transitions in grain boundaries, Acta Metall. 37 (1989) 2133–2139, https://doi.org/10.1016/0001-6160(89)90138-7.
[44] C.J.D. Hetherington, U. Dahmen, R. Kilaas, A.I. Kirkland, A.R.R. Meyer, D. L. Medlin, HREM analysis of Σ3 {112} boundaries in gold bicrystal films, in: Electron Microsc. Anal. Dundee, 168, CRC Press, 2001, pp. 59–62, 2001Philadelphia.
[45] A.D. Banadaki, S. Patala, A simple faceting model for the interfacial and cleavage energies of Σ3 grain boundaries in the complete boundary plane orientation space, Comput. Mater. Sci. 112 (2016) 147–160, https://doi.org/10.1016/j.commatsci.2015.09.062.
[46] Brink, T., Langenohl, L., Pemma, S., Liebscher, C.H., Dehm, G., Stable nanofacets in [111] tilt grain boundaries of face-centered cubic metals. arXiv (2023) 1–6. 10.48550/arXiv.2309.07595.
[47] D.L. Medlin, K. Hattar, J.A. Zimmerman, F. Abdeljawad, S.M. Foiles, Defect character at grain boundary facet junctions: analysis of an asymmetric $\Sigma = 5$ grain boundary in Fe, Acta Mater. 124 (2017) 383–396, https://doi.org/10.1016/j.actamat.2016.11.017.
[48] T. Frolov, D.L. Medlin, M. Asta, Dislocation content of grain boundary phase junctions and its relation to grain boundary excess properties, Phys. Rev. B 103 (2021) 1–14, https://doi.org/10.1103/PhysRevB.103.184108.
[49] N. Chistyakova, T.M.H. Tran, A study of the applicability of different types of interatomic potentials to compute elastic properties of metals with molecular dynamics methods, AIP Conf. Proc. (2016) 1772, https://doi.org/10.1063/1.4964599.
[50] M. Saito, Z. Wang, S. Tsukimoto, Y. Ikuhara, Local atomic structure of a near-sigma 5 tilt grain boundary in MgO, J. Mater. Sci. 48 (2013) 5470–5474, https://doi.org/10.1007/s10853-013-7340-7.
[51] M. Saito, Z. Wang, Y. Ikuhara, Selective impurity segregation at a near-$\sum$5 grain boundary in MgO, J. Mater. Sci. 49 (2014) 3956–3961, https://doi.org/10.1007/s10853-014-8016-7.
[52] T. Mitsuma, T. Tohei, N. Shibata, T. Mizoguchi, T. Yamamoto, Y. Ikuhara, Structures of a $\Sigma = 9$, [110]/{221} symmetrical tilt grain boundary in SrTiO3, J. Mater. Sci. 46 (2011) 4162–4168, https://doi.org/10.1007/s10853-011-5266-5.
[53] L. Li, R.D. Kamachali, Z. Li, Z. Zhang, Grain boundary energy effect on grain boundary segregation in an equiatomic high-entropy alloy, Phys. Rev. Mater. 4 (2020) 53603, https://doi.org/10.1103/PhysRevMaterials.4.053603.
[54] S.A. Bojarski, M.P. Harmer, G.S. Rohrer, Influence of grain boundary energy on the nucleation of complexion transitions, Scr. Mater. 88 (2014) 1–4, https://doi.org/10.1016/j.scriptamat.2014.06.016.
[55] S.A. Bojarski, J. Knighting, S.L. Ma, W. Lenthe, M.P. Harmer, G.S. Rohrer, The relationship between grain boundary energy, grain boundary complexion transitions, and grain size in Ca-doped Yttria, Mater. Sci. Forum. 753 (2013) 87–92, https://doi.org/10.4028/www.scientific.net/MSF.753.87.